

International Journal of Nanoelectronics and Materials

IJNeaM

ISSN 1985-5761 | E-ISSN 2232-1535



Role of ZnO-doping concentration on CuO thin film for promising NH_3 gas detectors application by a thermal vaporization method

Ahmed A. Jabber a *, Ali R. Abdulridha

- $\it aDepartment$ of Physics, College of Education for Pure Sciences, University of Babylon, Hilla 51002, Iraq
- *Corresponding author. Tel.: +9647838902542; e-mail: ahd090000@gmail.com

Received 03 March 2025, Revised 28 April 2025, Accepted 23 June 2025

ABSTRACT

This study included the fabrication of nanofilms of ZnO-doping concentration on CuO nanoparticles (NPs) by a thermal vaporization method. The film thickness is 50 ± 0.2 nm and is deposited on glass substrates at room temperature (RT). The deposited nanofilms exhibit no discernible peaks in X-ray diffraction (XRD) examination. The widening of the peak indicates a lack of long-range symmetry, resulting in a disordered nanocrystalline structure. This process yielded films with a homogeneous surface, as confirmed by atomic force microscope (AFM). As ZnO doping increased, roughness increased by 70.48%, the root mean square value increased by 72.55%, and the average grain diameter increased by 50.28%. The field emission scanning electron microscope (FESEM) analysis showed equally scattered CuO/ZnO nano-films. The optical characteristics of CuO/ZnO nano-films show ZnO presence. The absorbance and absorption coefficient are both increased. As ZnO concentrations increased, energy and transmittance band gaps reduced from 0.83 to 0.71 eV and 3.610 to 3.487 eV. The most significant reported sensitivity at RT to NH₃ at a concentration of 0.20 wt.% was 47.06% at an operating temperature of 100°C. This sensitivity was achieved within an answer time of 32.49 s, with a recuperation period of 29.61 s. The most excellent reported sensitivity at 573 K to NH₃ at a concentration of 0.20 wt.% was 45.05% at an operating temperature of 100°C achieved within an answer time of 33.75 s, with a recuperation period of 28.62 s and the most excellent reported sensitivity at 673 K to NH₃ at a concentration of 0.20 wt.% was 68.81% at operating temperature of 100°C achieved within an answer time of 27.81 s, with a recuperation period of 15.84 s, so that it is considered the best sensitivity for NH₃ detection. The sensitivity of the sample (0.20 wt.%) typically decreases as the temperature rises. This makes it seem like the gas-detector can interact with NH₃ gas without needing any activation energy and that the interaction is predicated on polarity and physical adsorption. Nevertheless, the sensitivity of the pure, 0.08, and 0.14 wt.% samples exhibited a positive correlation with temperature within a specific range. The findings regarding the structural and conductive characteristics of CuO/ZnO nano-films hold promising applications in advanced optoelectronic devices and gas sensors.

Keywords: Nanoparticles, Nano-films, Thermal vaporization, AFM, FE-SEM, Gas-detector

1. INTRODUCTION

Historically, the term nanomaterial has denoted items originating from nanotechnology. Since 1974, Professor Norio Taniguchi has characterized nanotechnology as silicon machining's straight expansion into dimensions less one micrometer [1]. Various international organizations and committees have proposed numerous definitions of the term "nanomaterial" in recent years, all of which have indicated an upper dimension limit of 100 nm [2]. Nanomaterials can demonstrate distinctive physical and chemical characteristics that are not present in their bulk counterparts. The reduction of scale is a critical characteristic that differentiates nanomaterials from conventional materials, resulting in materials with distinctive properties that are a direct consequence of their nanoscale dimensions. The most apparent result of scale reduction is the significantly increased surface area per unit mass or specific surface area [3]. An increase in surface area implies the presence of additional surface atoms. An increase in surface area will lead to a more significant number of atoms with unresolved bonds and lower coordination because, compared to atoms in bulk, surface

atoms have fewer partners. Because surface atoms are often less stable than bulk atoms, the surface of nanomaterials is more reactive than their bulk counterparts [4].

Nanocomposites can be made in many ways, including chemical, physical, biological, etc. Nanomaterials' unique and customizable features have fascinated researchers throughout the globe, and their potential is being studied in disciplines such as medical treatments and diagnostics, drug transport, antibacterial nanomedicine, photocatalysis, catalysis, and energy generation [5-7]. Metal oxides have shown to be quite useful in a range of applications as a result of their capacity to absorb light [8]. As a result, the deposition of these metal oxide nanoparticles onto glass substrates and other natural surfaces. Metal and metal oxide nanoparticles are utilized in a variety of fields, including environmental remediation, molecular detection, and catalysis [9]. Many uses have been researched for metal oxides [10]. Early transition metal-derived metal oxides showed remarkable capabilities, including catalytic, electro-optic, electromechanical, ferroelectric, and wave density charging characteristics [11, 12].

The scientific community has become more interested in recent efforts to produce semiconductor oxide materials. Because of its optical and electrical characteristics, copper(II) oxide (CuO) is an auspicious material due to its photochemical photoconductive and properties. It demonstrates p-type semi-conductivity, with a 3 to 3.62 eV band gap and modest electrical resistance values. When CuO is exposed to reducing-gas species, its electrical conductivity decreases [13-15]. The use of CuO is recognized when it comes to technology significant material due to its various uses in advanced science and technology, such gas-detectors [16], sun photovoltaics, heterogeneous catalysis, lithium-ion electrodes, hightemperature superconductors, and field emission emitters [17].

Zinc oxide (ZnO) is a well-known n-type semiconducting oxide widely used for reducing gases within the operating range of 273-443 K. This oxide material is comparatively low in operating temperature and exhibits high reactivity toward reducing gases. It is also capable of readily adsorbing. Because of its stable phase, cheap cost, and inherent non-stoichiometry, it contains oxygen on its surface. Furthermore, it is easy to use. ZnO is produced annually at around 1.5 million tons and has been utilized throughout history [18]. ZnO is stable, piezoelectric, and optically excellent. These technologies include transparent conductive materials, surface acoustic wave devices, piezoelectric transducer materials, Gas Detectors, and photovoltaic cells. Recent electronic innovations have a few promising applications [19]. Thin ZnO sensors, made from high-band gap oxide semiconductors, have the potential to detect certain lights and gases. Regarding complex applications such as window layers, ZnO is widely used as a transparent conducting oxide in heterojunction solar cells, heat mirrors, and piezoelectric devices. Heterojunction formation in ZnO-based catalysts. ZnO has a high direct optical energy gap of 3.3 eV, mainly allowing solar radiation to pass through it. In addition, the plentiful presence of ZnO in nature reduces its expense, and its strong ability to block UV radiation allows for its utilization in various products and procedures [20]. In recent years, many studies have explored the use of CuO and ZnO nanoparticles for Gas-Detector applications [21–24].

Population development in recent decades has spurred the swift expansion of automobile transportation and industry. Consequently, hazardous and poisonous chemical species are becoming commonplace in daily life, posing a significant threat to the environment and human health [25, 26]. Invasive species are frequently the most challenging to observe because they cannot be observed, tasted, or touched. Gas sensing technology attracts interest in both primary and industrial domains for dependable air quality monitoring [27]. There are numerous classifications of gas detectors, and the criteria vary. Gas detectors can be classified according to the interaction between the gas and the gas sensing material, the type of sensing material utilized, or the material's overall sensing process. Among these categories are sensors for gases in semiconductors [28, 29]. Sensors for solid electrolyte gas [30], optical gas detectors, gas detectors that use contact combustion, gas detectors that use quartz vibrators, and gas detectors that use surface acoustic waves [31]. Research has shifted its attention to gas-detectors that use different metal oxide semiconductors (MOS) as sensing layers, as opposed to other sensors, because of their superior sensitivity, compact size, and low cost [32].

This study used the thermal vaporization method to study CuO/ZnO nano-films. Research into CuO/ZnO sensors for detecting NH_3 gas is, as far as we know, underdeveloped. By adjusting the ZnO to CuO concentration ratio, nano-films of CuO/ZnO were effectively created. The research found that morphological development, which promotes NH_3 gas reaction, is triggered by variations in concentration. Plus, we ran the enhanced gas sensing capabilities through their paces to see how well they detected ammonia (NH_3) . The nano-films of (CuO/ZnO) used in this investigation show promise for NH_3 gas detection.

2. MATERIALS AND METHODS

ZnO-doped CuO thin films with varying concentrations (0.08, 0.14, and 0.20 wt.%) have been fabricated using the thermal evaporation technique on glass substrates. The films were applied to 50 ± 0.2 nm thick glass substrates at room temperature (RT). The Edward C-306 deposition system uses thermal evaporation. The molybdenum boat used CuO and ZnO powder, purified 99.9%. An orderly evacuation of the chamber was executed at 1×10^{-7} bar with a temperature of 1100° C (the boiling point of CuO nanoparticles in the air is 2000° C), while the glass substrates were kept at ambient temperature. The substrates were positioned approximately 15 cm from the source to ensure that the evaporated flux would impinge upon them at an angle and a 0.3 nm/sec deposition rate.

Methods like morphology and structure will be examined to analyze the samples using X-ray diffraction (XRD), a field emission scanning electron microscope (FESEM), and an atomic force microscope (AFM). Various tests were used to assess the optical characteristics of nano-films, including band gaps (E_g), absorbance (A), transmittance (T), and absorbance coefficient (α). A spectrophotometer fitted with two laser beams covering the wavelength span between 320 and 720 nanometers (Shimadzu, UV-1800 A0, Japan) was used to carry out these tests. Additionally, we looked into and examined the DC nano-films' electrical properties. Using a Keithley 2400 electrometer allowed for the acquisition of specific temperature values.

The sensing properties of thin films of CuO/ZnO were assessed under the influence of a fluctuating flow of NH_3 gas. Gas flow rate was 0.5 liter/min NH_3 concentration was 150 ppm. The sensor response to ammonia gas (NH_3) was measured using a resistance-based measurement method. The changes in the sensor's electrical resistance were monitored before, during, and after exposure to ammonia gas at a concentration of 150 ppm. An increase or decrease in resistance was recorded as an indicator of the sensor's sensitivity and response. A precision resistance

measurement device, via a digital multimeter, was used to continuously record the sensor's resistance throughout the experimental period. The baseline conditions were maintained at a temperature of 25 ± 2°C and a relative humidity of $40 \pm 5\%$. Clean air free of ammonia was used as the baseline reference for measuring the sensor response. To ensure repeatability of the results, the tests were repeated 3 consecutive times under identical conditions, allowing the sensor to return to baseline conditions between each measurement. The gas-detector system includes a stainless-steel cylindrical examination chamber with a diameter of 20 cm and a height of 10 cm, which is subsequently evacuated by a rotary pump. The test chamber is after being attached to the heater, the sensor is turned on. The basic electrical connections between the thermocouple, the pin feed-through, and the spring-loaded pins of the sensor have been established. There is a hermetically enclosed testing room. The test chamber is then evacuated to a pressure of around 1×10^{-1} bar using a rotary pump. A temperature controller is used to calculate the sensor's required operating temperature. The needle valves are used to regulate the flow rate of the test gas and carrier (air) flow meters. By opening the two-way valve, the gas with a known concentration in the mixing chamber is allowed to enter the test chamber. Two flow meters track the air mixing ratio while the sensor's resistance fluctuation is recorded at a predefined test gas concentration. To enable the sensor to return to the baseline current value R_0 , the test gas' needle valve is closed after the measurement. For the additional required temperatures, the previously specified measurements are repeated. Figure 1 depicts the gasdetector testing setup. Figure 2 illustrates the gas sensor system used.

The absorbance equation represents the proportion of the light intensity absorbed by a substance (I_A) to the light intensity that is incident on the material (I_0) [33]:

$$A = I_A/I_0 \tag{1}$$

Transmittance is the ratio of beam intensity transmitted through the film to incident beam intensity on the film, represented by the equation [34]:

$$T = I_T/I_0 (2)$$

where T is the transmittance, I_T is the intensity of transmitted light and I_0 is the incident light intensity.

The absorption coefficient propagation is the ratio of the decrease in incoming radiation's energy flow per unit distance in the wave's direction. Centimeter inverse (cm⁻¹) serves as the unit of measurement for the absorption coefficient [35]:

$$\alpha = 2.303 \left(\frac{A}{t}\right) \tag{3}$$



Figure 1. Gas sensing apparatus

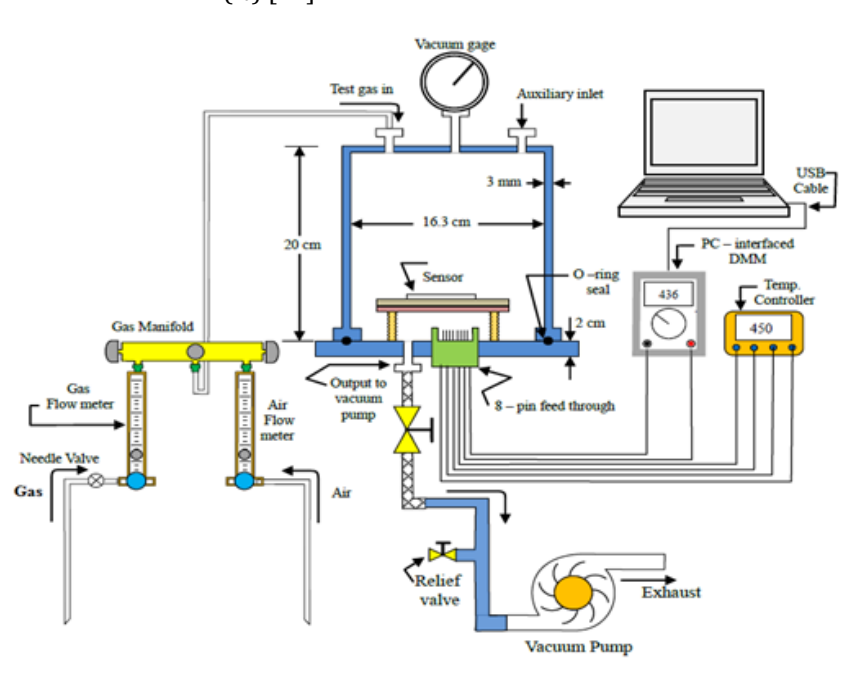


Figure 2. Gas sensing apparatus schematic diagram

Jabber et al. / Role of ZnO-doping concentration on CuO thin film for promising NH₃ gas detectors application by a thermal vaporization method

The fundamental absorption edge is one of the most remarkable characteristics of a semiconductor's absorption spectrum. It is equivalent to the energy band separation between the upper valence band (V.B.) and the bottom conduction band (C.B.) and can be calculated equation [36]:

$$\alpha h v = B \left(h v - E_q^{opt} \right)^r \tag{4}$$

where α is the absorption coefficient, h is the Blanck's constant, v is the light frequency, B is the material-dependent Constant and E_g^{opt} is the optical band gap.

The quality in question is measured by the electrical conductivity of direct current, which is written as $\sigma_{D.C}$ [37]:

$$\sigma_{D.C.} = 1/\rho = L/RA \tag{5}$$

where $\sigma_{D.C.}$ is the direct current electrical conductivity, ρ is the electrical resistivity, L is the length, R is the electrical resistance and A is the cross-sectional area.

The activation energy can be ascertained via calculation [38, 39]:

$$\sigma_{D.C.} = \sigma_o \exp - (E_{act}/K_B T_B) \tag{6}$$

In this case, σ represents electrical conductivity that is particular to temperature. E_{act} stands for activation energy, K_B for the Boltzmann constant, T_B for temperature and σ_0 for electrical conductivity at absolute zero.

The sensor response (S) is the ratio of the variation in resistance ($R_g - R_a$) when exposed to target analytics to the sensor's ambient resistance (R_a)[40].

$$S(\%) = \frac{R_a - R_g}{R_g} \times 100\% \tag{7}$$

 R_g and R_a denote the resistances of the sensor when subjected to analyte gas and air, respectively.

Both the reaction and recovery times curves are determined by calculating the time it takes for the system to respond and recover at severe operating temperatures ranging from RT to 200°C, using specific equations [41, 42]:

Response time =
$$|t_{gas (on)} - t_{gas (off)}| \times 0.9$$
 (8)

Recover time =
$$|t_{gas (off)} - t_{gas (recover)}| \times 0.9$$
 (9)

3. RESULTS AND DISCUSSIONS

3.1. X-ray Diffraction Analysis

XRD analysis was used to ascertain the structure and crystallinity of the produced films. Figure 3 illustrates the XRD patterns of CuO/ZnO nanofilms deposited on glass substrates. The XRD data reveals that the CuO/ZnO nanofilms exhibit no distinct peaks, indicating inadequate crystallization of the nanofilms [43]. The breadth shown in Figure 3 pertains to the peak widening resulting from the

diminutive particle size. The ambiguity in the microstructure of ZnO-doped CuO nanofilm arises from the restricted periodic area in atomic arrangements that provide identical diffraction peak profiles. Peak broadening is seen when the sample undergoes plastic deformation, resulting in warped lattice planes that alter the spacing of specific sets across different grains or between various sections of a single grain [44]. The amorphous form originated from the very small particles [45].

3.2. Atomic Force Microscope (AFM) Measurements of CuO/ZnO Nanocomposites

Figure 4 shows that the CuO nanofilm was impregnated with pure CuO and ZnO at RT weight ratios (0.08, 0.14, and 0.20%). The AFM images of the pure CuO and ZnO nanofilm exhibit consistent granular surface shape and consistent distribution and dispersion of ZnO particles inside the CuO matrix. Moreover, the AFM images of the nanofilm revealed a clear, smooth surface morphology consisting of tiny grains of the prepared films. Increased ZnO nanoparticle concentration increases film crystallinity and grain size. As the concentration of ZnO nanoparticles rose from 0.08 wt.% to 0.20 wt.%, the AFM picture showed an increase in grain size from 1.01 to 4.82 nm. Film surface roughness is shown as root mean square (RMS) values in Table 1. With increasing ZnO nanoparticle concentration, the average root mean square (RMS) roughness rises from 0.174 to 0.634 nm [46].

3.3. Field Emission Scanning Electron Microscope (FESEM) Measurements of CuO/ZnO Nanocomposites

Figure 5 shows the FESEM images used to study the surface morphology of CuO/ZnO nanofilms at a scale of 500 nm. The micrographs were analyzed to assess the morphological and surface characteristics of the produced CuO and CuO nanocomposites. The morphological changes in CuO due to

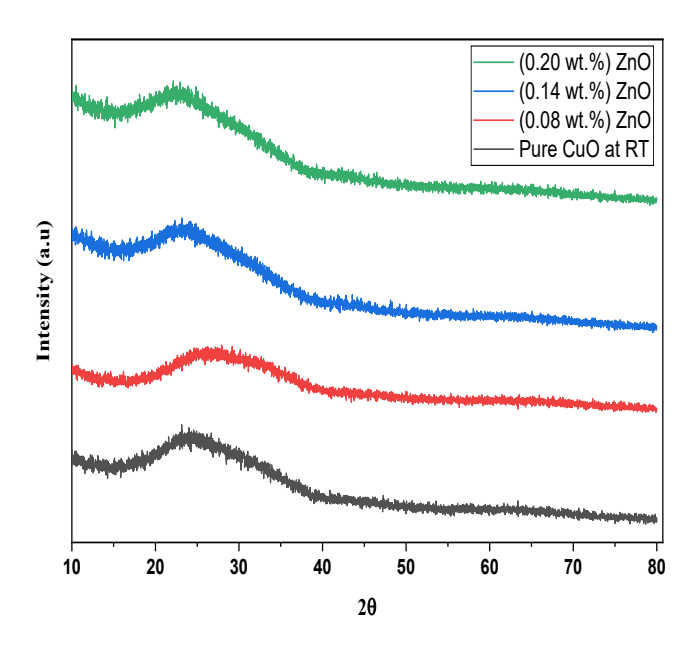


Figure 3. XRD of CuO/ZnO nanofilms

the addition of ZnO show that the concentration of ZnO ions significantly affects the crystal growth rate of CuO nanomaterials [47]. The shape of nanomaterials can be controlled by adjusting the kinetics of crystal formation, which is significantly influenced by the presence of other ions. In the CuO/ZnO nanocomposite system, ZnO helps refine the surface of CuO nanoparticles. With an increased concentration of ZnO ions, surface energy is reduced through self-aggregation. At lower chemical concentrations, nanoparticles tend to aggregate, supporting these observations. Moreover, the interaction between CuO and ZnO nanoparticles promotes the formation of a connected network. Initially, the size of the nanoparticles increases as the ZnO content rises. This is attributed to the aggregation and crystalline growth triggered by the higher ZnO concentration, leading to larger and more refined structures at specific concentrations [48, 49].

3.4. Optical Characteristics of CuO/ZnO Nanofilms

Figure 6 A displays the ultraviolet-visible (UV-Vis) spectra of the CuO and ZnO nanomaterials. The absorbance of all the samples was measured throughout the wavelength range of 320–720 nm. The absorbance of nanomaterial is influenced

by various parameters, including layer thickness, dislocation density, micro-strain, oxygen vacancies, impurity centers, and particle size [50]. CuO/ZnO absorption with variable concentration of ZnO and wavelength range at normal temperature. CuO/ZnO optical absorption varies with wavelength, as shown in Figure 6. These statistics imply that all films have higher UV absorption spectra. The nanocomposites exhibit a noticeable lack of absorbance in the visible spectrum. To provide further elucidation, we can approach this matter from the following perspective: Photons of high frequencies do not undergo interactions with atoms, resulting in their transmission rather than obstruction. Substances around the fundamental absorption edge absorb photons as light wavelength decreases. Increasing ZnO weight percentages boosts absorption. This happens because unbound electrons absorb light. These results match those of other researchers [50]. These measurements are vital for understanding how the material interacts with light, which helps determine its electronic properties and estimate film thickness. Additionally, absorption data is essential in calculating the energy band gap, a key parameter in evaluating the material's suitability for optoelectronic applications [51].

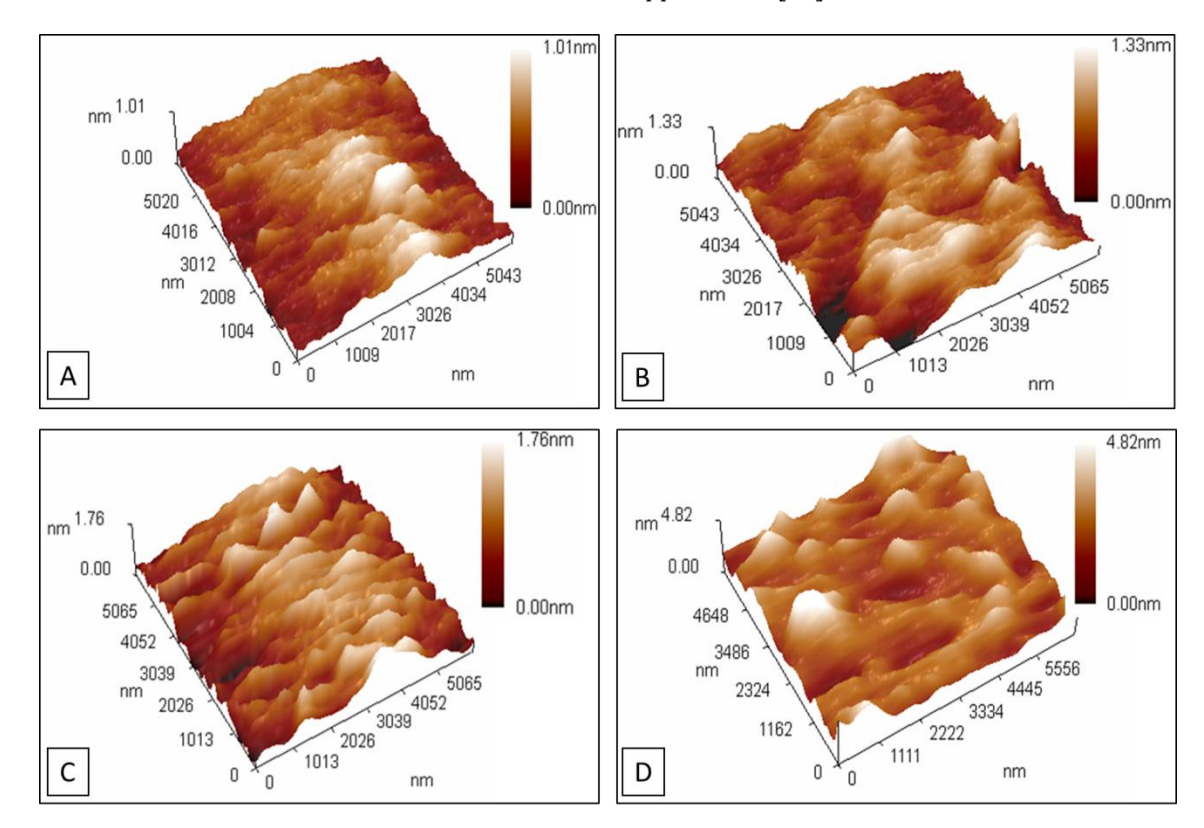


Figure 4. The AFM surface morphology of CuO/ZnOnanofilms. A: pure CuO, B: 0.8 wt.% ZnO nanoparticles, C: 0.14 wt.% ZnO nanoparticles, and D: 0.20 wt.% ZnO nanoparticles at room temperature

Table 1. Morphological characteristics at RT CuO/ZnO nanofilms

ZnO-doped CuO Con. of wt.%	Root mean square Sq (nm)	Roughness average Sa (nm)	Ten-point heigh Sz (nm)	Average diameter (nm)
Pure (CuO)	0.174	0.139	0.749	359.9
0.08 wt.% ZnO	0.232	0.185	1.010	360.3
0.14 wt.% ZnO	0.326	0.263	1.400	476.2
0.20 wt.% ZnO	0.634	0.471	2.630	723.9

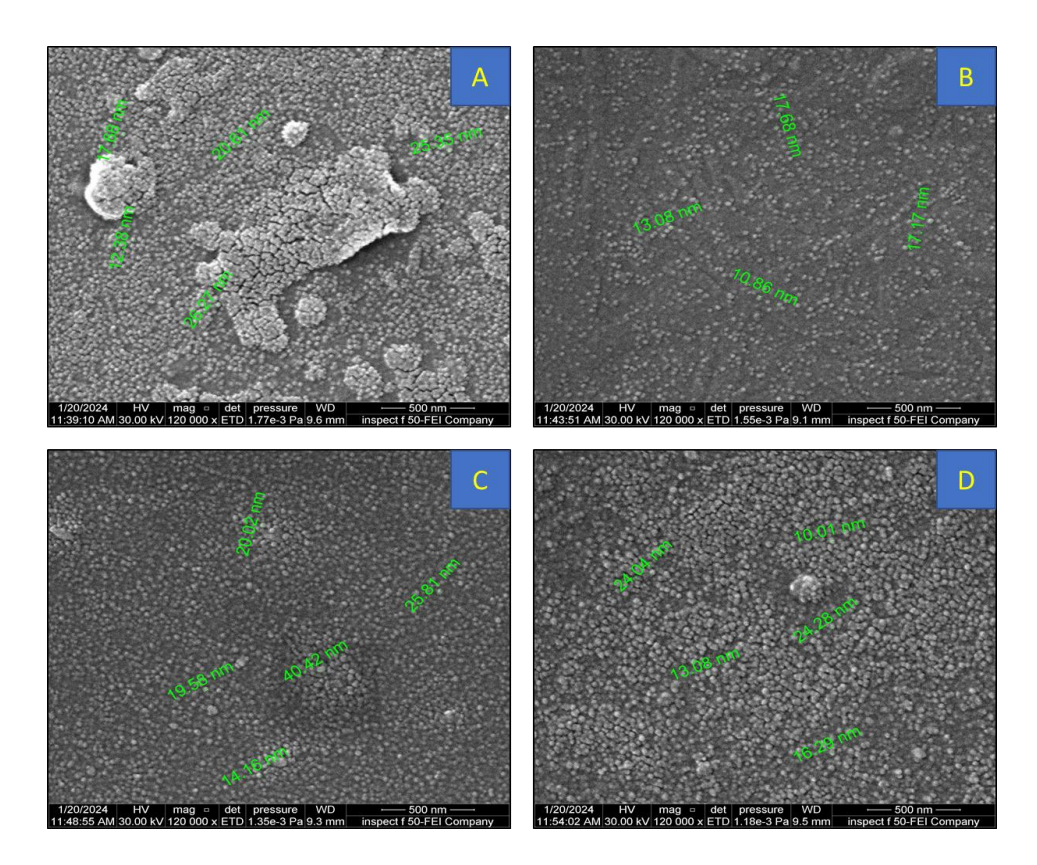


Figure 5. FESEM images of CuO/ZnO NCs: A pure B: 0.08 wt.% ZnO, C: 0.14 wt.% ZnO, and D: 0.20 wt.% ZnO at RT

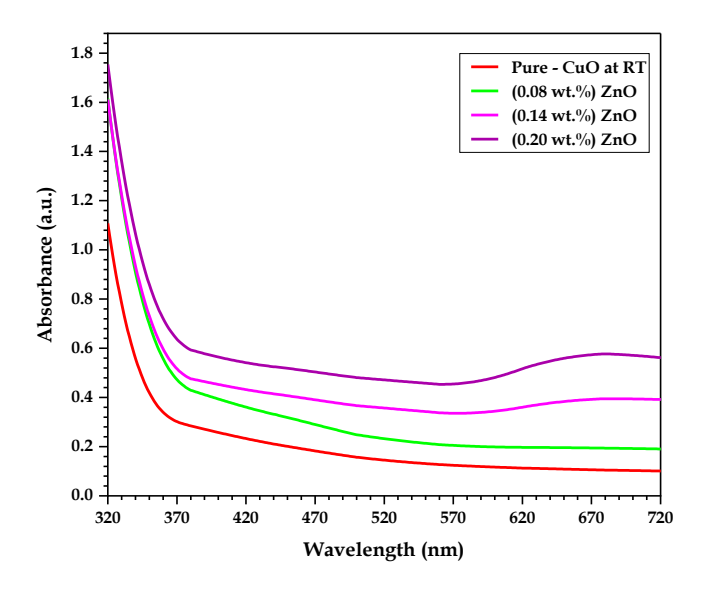


Figure 6. The absorbance spectra of CuO/ZnO nanofilms with respect to wavelength

The wavelength-dependent transmittance (T) of CuO/ZnO nanofilms is shown in Figure 7. The optical transmittance spectrum for nanofilms with various ZnO composition nanoparticle concentrations was examined. wavelength-transmittance relationship is obvious since ZnO nano-doping concentration impacts transmittance. Specifically, when the wavelength increases, transmittance also increases, while the transmittance decreases with ZnO concentration increasing nano-doping. The outcomes presented here align with the findings of another researcher [52]. The development of scattering and reduced oxygen vacancies at grain boundaries

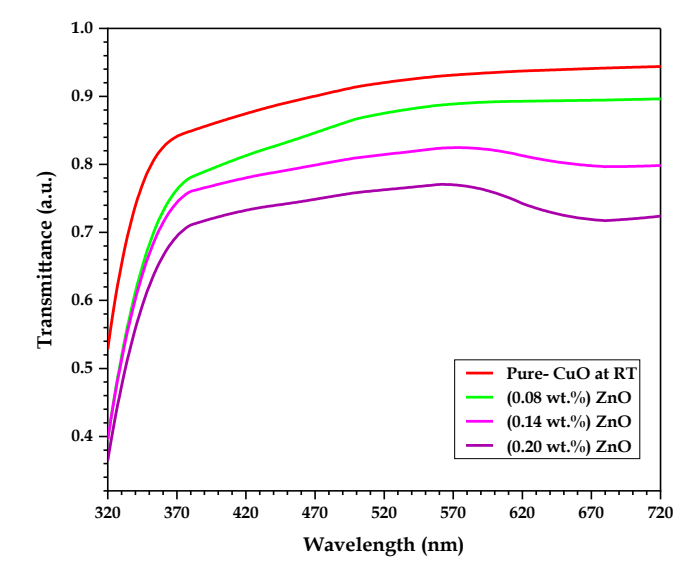


Figure 7. Plot of transmittance spectra vs wavelength of CuO/ZnO nanofilms

transmission. Nevertheless, the films' absorbance might fluctuate due to variables like particle size, oxygen deprivation, and flaws in grain structures, which are influenced by the doping components [36].

Figure 8 illustrates the absorption coefficient about a wavelength for CuO/ZnO nanofilms. Longer wavelengths have the lowest absorption coefficient and related energy levels. An electron within a semiconductor, either as an atom or an ion. The inadequate photon's energy inhibits the transport of electrons conduction to valence band transition [53].

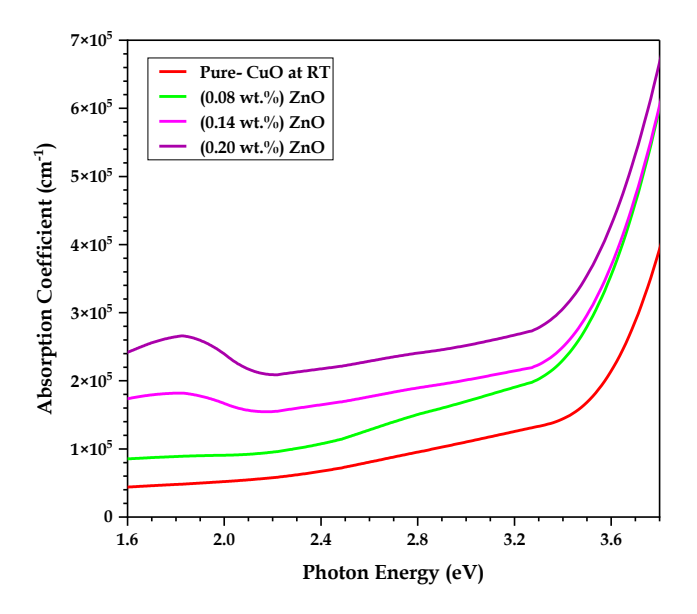


Figure 8. The absorption coefficient spectra of nanofilms composed of CuO/ZnO as a function of wavelength

Maximizing high-energy absorption increases the probability of electron transitions. Consequently, the photon's energy is adequate to change the valence band electron from the conduction band. The seen photon's energy exceeded the allowed energy limit. This coefficient runs higher than the absorption coefficient during direct electron transitions; hence, at elevated energies ($\alpha > 10^4$ cm⁻¹), electrons and photons retain their momentum and energy while traversing the transition. Low-energy When the absorption coefficient is less than 10^4 cm⁻¹, indirect electron transmission is likely. Phonons facilitate the maintenance of electron trajectories. The absorbance coefficient of the CuO/ZnO thin layer exceeds 10^4 cm⁻¹ [54].

One of the outcomes is that the absorption coefficient of the thin film of CuO/ZnO is larger than $10^4~\text{cm}^{-1}$. This demonstrates that electron exchanges occur in a straightforward manner.

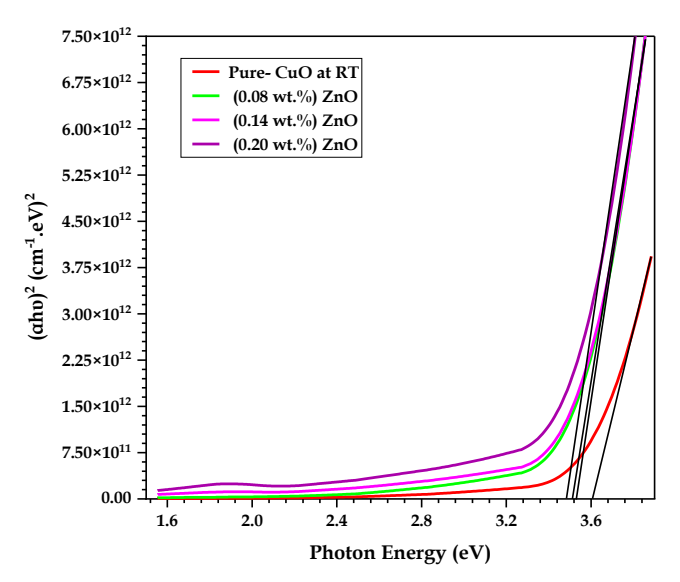


Figure 9. A plot of (αhυ)² vs. photon energy (hυ) for CuO/ZnO nanofilms at various ZnO doping ratios

Glass samples' optical band gap can be calculated using Equation (4) [36], where B represents a constant, while hu represents the energy of the incident photon. The optical transitions (n = 2, 1/2, 3, and 1/3) can be classified as either indirect allowed, direct allowed, prohibited indirect, or forbidden direct transitions The band gap for the allowed and forbidden direct transition was determined using UV-Vis absorption spectroscopy, where the absorption curves were analyzed, and Tauc plots were drawn to extract the band gap value. The significance of the energy band gap lies in its direct impact on the electronic and optical properties of the nanofilm and, consequently, on the efficiency of gas sensing. Doping with ZnO alters the band gap, which leads to an improved film response to specific gases by enhancing electrical conductivity and surface sensitivity, making the material promising for gas detector applications [55]. Figure 9 shows the absorption edge (hu)2 for CuO/ZnO, which correlates with a photon's energy. The energy gap between pure CuO and ZnO-doped CuO at various weight ratios (0.08, 0.14, and 0.20) with a thickness of 50 nm is shown by extrapolating the $(hu)^2 = 0$ value from the top half of the curve to the x-axis. As the ZnO ratio rises, the energy gap values are observed to decrease significantly. The band gap values for the generated nanofilm reduced from 3.610 to 3.487 eV for allowed direct transitions and from 3.418 to 3.200 eV for authorized indirect transitions The Burstein-Moss effect, which occurs in semiconductor films where the Fermi level is located within the conductive band and acts as an electron shield to promote electron transmission, explains how CuO/ZnO valence band electrons are moved to conduction band electrons. The listed Eg values may be found in Table 2. This study's results are pretty similar to those of the second researcher [56].

Figure 10 shows the forbidden transition of the direct energy gap between CuO and ZnO, and Table 2 explains the determined barred transition. These outcomes meet the researcher's expectations [57].

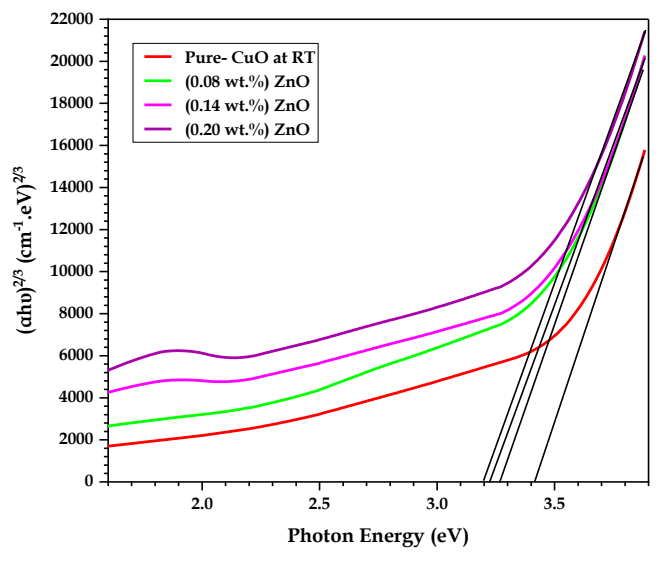


Figure 10. A plot of $(\alpha h \upsilon)^{2/3}$ vs. photon energy (h υ) for CuO/ZnO nanofilms at various ZnO doping ratios

Table 2. The energy gap values for permissible and forbidden direct transitions in (CuO/ZnO) nano-films

CuO-doped ZnO (wt.%)	Eg of Allowed (eV)	Eg of Forbidden (eV)
Pure (CuO)	3.610	3.418
0.08 wt.% ZnO	3.537	3.272
0.14 wt.% ZnO	3.512	3.228
0.20 wt.% ZnO	3.487	3.200

3.5. DC-Electrical Characteristics of CuO/ZnO Nanofilms

The study of electrical properties of nanomaterials is of great importance as it impacts their applications in electronics and sensors. In the case of the CuO/ZnO nanocomposites, the DC conductivity depends on several factors such as particle size, structural composition, quantum effects, and temperature. In nanomaterials such as CuO/ZnO, electrical conductivity depends on the type of charge carriers and their transport across the boundaries of the nanostructures. ZnO is an n-type semiconductor due to the presence of electrons as the primary charge carriers. At the same time, CuO is a p-type semiconductor due to the presence of holes as the primary charge carriers. When the nanocomposites are formed, a heterojunction p-n forms between the two materials, which affects the electrical properties of direct current. Combining CuO with ZnO improves the electrical properties due to the p-n junction effect, making it suitable for sensor devices, transistors, and modern semiconductors [58].

Figure 11 illustrates the temperature-dependent variation in electrical conductivity of CuO/ZnO nanofilms. At low temperatures, the movement of charge carriers is restricted due to barriers caused by grain boundaries and low thermal energy, leading to high electrical resistance. As temperature

3.5×10⁻⁷

3.0×10⁻⁷

2.5×10⁻⁷

2.5×10⁻⁷

1.0×10⁻⁷

1.0×10⁻⁷

5.0×10⁻⁸

1.5x10⁻⁷

1.0x10⁻⁷

Temperture (°C)

Figure 11. The correlation between temperature and the thinfilm electrical conductivity of direct current (D.C.) comprised of CuO/ZnO nanofilms

increases, the thermal energy of the charge carriers increases, facilitating their movement across the barriers, and thus, conductivity improves [59].

Figure 12 depicts the correlation between the ZnO nanoparticle concentration in samples and the electrical conductivity of the surface when exposed to direct current. The results of this study show a positive relationship between DC electrical conductivity and ZnO concentration. This results from a persistent network of ZnO nanoparticles forming inside the thin layers. These nanoparticles possess channels that facilitate the movement of charge carriers inside the material, accounting for this outcome. ZnO nanoparticles can enhance conductivity by improving the connectivity between CuO particles and increasing the charge carrier density. The increase in filler material is directly correlated with the growth in the number of charge transporters [60].

Figure 13 shows the relationship between the reciprocal of the absolute temperature and the natural logarithm of the standard deviation of direct current conductivity (Ln σ_{DC}) CuO/ZnO nanofilms [58]. When plotting Ln $\sigma_{D,C}$ vs. 1000/T, a straight line with a negative slope is obtained, indicating that conductivity increases with increasing temperature, as expected in semiconductors. From the slope of the line, the activation energy, Ea can be calculated, which reflects the energy required for electron or hole transport in the material. Changes in the slope at different temperature regions may indicate a shift in the conduction mechanism, such as a transition from band conduction to a hopping conduction mechanism. We conclude. The relationship between $Ln(\sigma_{D.C})$ and 1/T in CuO/ZnO nanofilms reflects semiconductor behavior, where conductivity increases with temperature. ZnO concentration may influence this relationship, leading to variations in electronic conduction mechanisms, particularly in nanostructured or amorphous films.

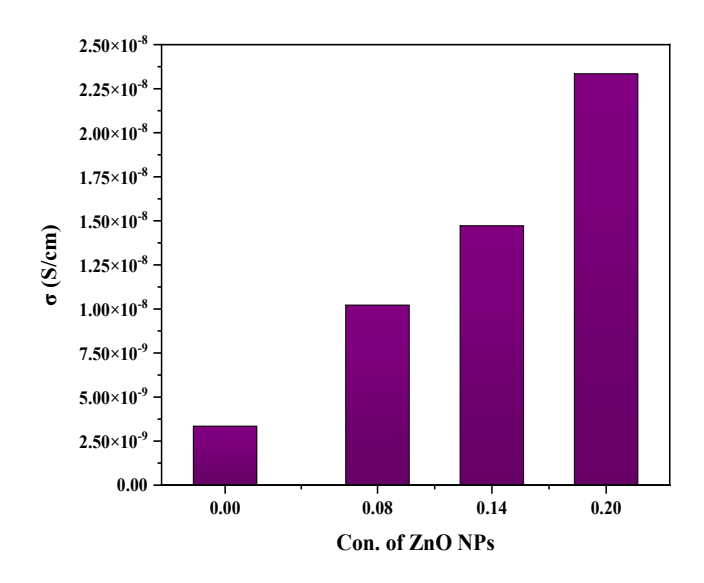


Figure 12. The correlation between the ZnO nanoparticle concentration and the thin-film electrical conductivity of direct current (DC) comprised of CuO/ZnO nanofilms

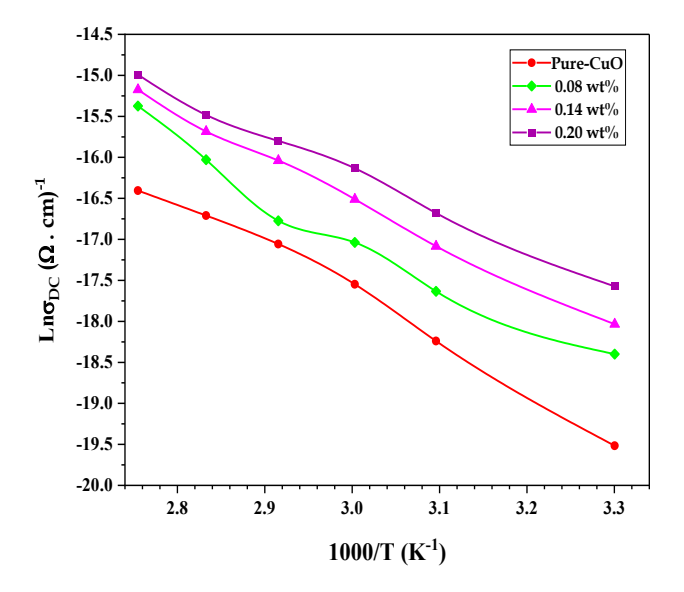


Figure 13. The correlation between the natural logarithm of electrical conductivity (Ln σ) and the reciprocal of absolute temperature of CuO/ZnO nanofilms

Figure 14 illustrates that the activation energy can be calculated using Equation (6), which relates electrical conductivity to temperature through the Arrhenius equation. Experimental results show that the activation energy of CuO/ZnO thin films ranges from 0.502 eV to 0.402 eV, influenced by ZnO doping concentration. As ZnO nanoparticle concentration increases, the activation energy decreases, indicating enhanced conductivity. This is due to the formation of localized energy states within the bandgap, which serve as traps for charge carriers and reduce the energy required for their excitation. Additionally, higher doping levels improve crystallinity and reduce structural defects, facilitating more efficient transportation of charges. ZnO also introduces donor levels, enhancing electron mobility. Consequently, the films require less thermal energy to activate charge carriers. This behavior is critical for gas sensors, where fast and sensitive response is essential. The trend confirms the potential of CuO/ZnO films in advanced sensing applications [61].

3.6. Application of CuO/ZnO Nanofilms as Gas-Detectors

Sensitivity (S%), sometimes called the response, was computed using Equation (7). Figure 15 indicates that at room temperature, before annealing, the most incredible sensitivity to NH₃ was obtained at 47.29% for a concentration of 0.20 wt.%, with a reaction time of 32.49 seconds and a recovery time of 29.61 seconds. In Figure 16, at 573 K, the maximum sensitivity recorded to NH₃ was 47.06% for the 0.20 wt.% sample, with a reaction time of 36 seconds and a recovery time of 19.8 seconds after annealing. Figure 17 illustrates that at 673 K, after annealing, the maximum sensitivity to NH₃ measured was 68.81% for a 0.20 wt.% concentration, with a reaction time of 27.81 seconds and a recovery time of 15.84 seconds. The sensitivity typically diminishes with increasing temperature for the sample (0.20 wt.%). This signifies that

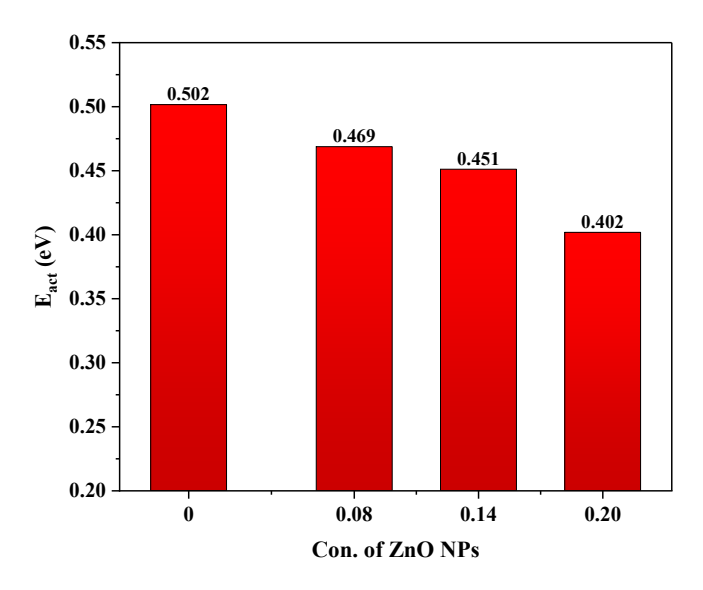


Figure 14. The relationship between ZnO nanoparticle concentration (wt.%) and activation energy for direct current (DC) electrical conductivity in CuO/ZnO nanofilms

physical adsorption and polarity are involved in the interaction and that the gas-detector does not need activation energy to interact with NH_3 gas. This activity is consistent with prior investigations [40]. For the (pure, 0.08, and 0.14) wt.% samples, temperature within a specified range resulted in an increase in sensitivity. This suggests that the gas-detector has achieved a high level of sensitivity and requires energy to establish contact with NH_3 gas [62].

The maximum sensitivity of pure CuO at room temperature (before annealing) was 16.6% at 100° C, with corresponding sensitivities of 28.17% at 0.08 and 37.61% at 0.14. After annealing at 573 K, the maximum sensitivity increased to 20.94% at 100° C, while the sensitivities at 0.08 and 0.14 were 29.95% and 37.47%, respectively.

The maximum sensitivity of pure CuO after annealing at 673 K was 19.37% at 100°C, with sensitivities of 34.43% at 0.08 and 48.21% at 0.14. The increase in operating temperature activated a thermally stimulated process, enhancing gas adsorption as a result of stronger interactions between the gas molecules and the material's surface. This behavior suggests improved chemical interactions at elevated temperatures, likely due to the increased mobility of $\rm NH_3$ molecules, which facilitates more effective surface adsorption in the sensor. Furthermore, sensitivity improved with higher sample concentrations, where increasing the nanoparticle content from pure CuO to 0.20 wt.% contributed to stabilizing or enhancing sensitivity at elevated temperatures.

The increase in chemisorbed NH_3 led to enhanced desorption rates, underscoring the significance of ZnO in offering potential active sites for NH_3 adsorption and thermal stability. Nonetheless, at elevated concentrations, the increase in sensing capabilities may be attributed to NH_3 chemical or physical adsorption, as seen in it.

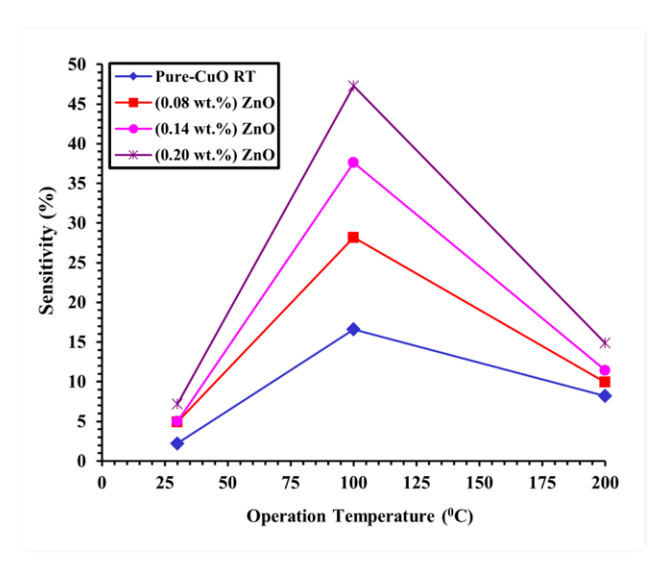


Figure 15. The sensitivity of CuO/ZnO nanofilms at 500 ppm for NH₃ Gas-detectors is plotted against operation temperature at RT

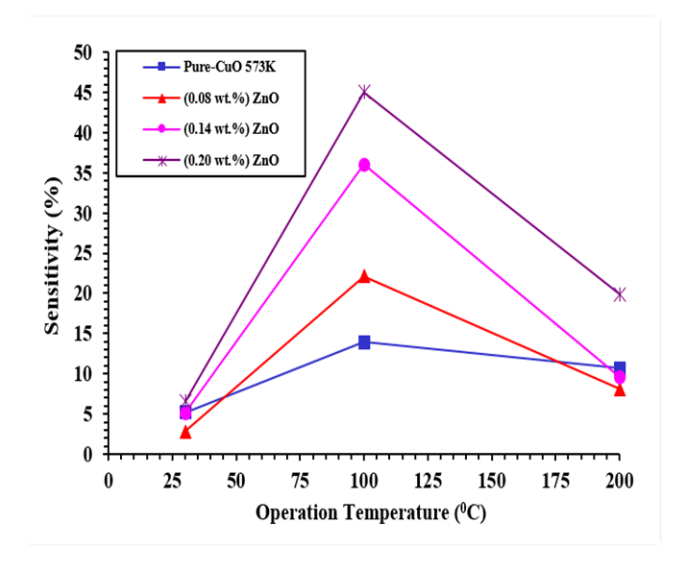


Figure 16. The sensitivity of CuO/ZnO nanofilms at 500 ppm for $\rm NH_3$ Gas-detectors is plotted against operation temperature at 573 K

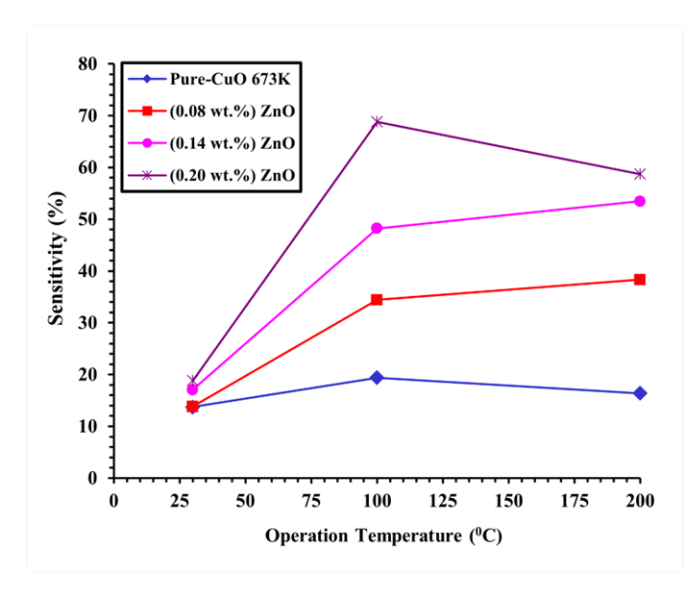


Figure 17. The sensitivity of CuO/ZnO nanofilms at 500 ppm for $\rm NH_3$ Gas-detectors is plotted against operation temperature at 673 K

Figures 18, 19, and 20 illustrate the correlation. The correlation between response and recovery time is shown at three operating temperatures. In Figure 18, the rapid response time (19 s) for the 0.14 wt.% sample at a temperature of 200°C for NH₃ gas is notably brief. The sample resistance takes around 36 seconds to return to normal—the prolonged reaction time of 200 s for the 0.20 wt.% sample may suggest that the gas-detector requires energy to initiate interacting with NH₃ gas. Conversely, it demonstrates that the recovery period for NH₃ test gas escalates with rising operating temperature [40].

Recovery periods fluctuate inconsistently throughout the samples and temperature conditions, as seen in Tables 3, 4, and 5. The time required to return to normal resistance after replenishment is known as the recovery time. The longest recovery time for the 0.20 wt.% sample is 44.91 seconds at 200°C. The 0.20 percent sample's prolonged recovery time at 200°C raises the possibility of changes to the sensor surface or chemical conditions that impede desorption. The longest recovery time in Figure 19 is 41.58 s at room temperature for the (0.08 wt.% at 573 K) sample, and in Figure 20, the longest recovery time is 42.75 s at 100°C for the (pure-CuO at 673 K) sample, as depicted in Tables 5 and 6.

Response and recovery times are essential performance indicators for NH_3 gas sensors based on CuO/ZnO thin films. The response time represents how quickly the sensor detects the presence of ammonia, while the recovery time indicates the speed at which it returns to its initial state after the gas is removed. Shorter times are especially important for real-time monitoring and rapid detection in industrial and environmental applications. CuO/ZnO hetero structures, with their p-n junctions, promote efficient charge transfer and enhance interactions with NH_3 molecules. These properties lead to faster adsorption and

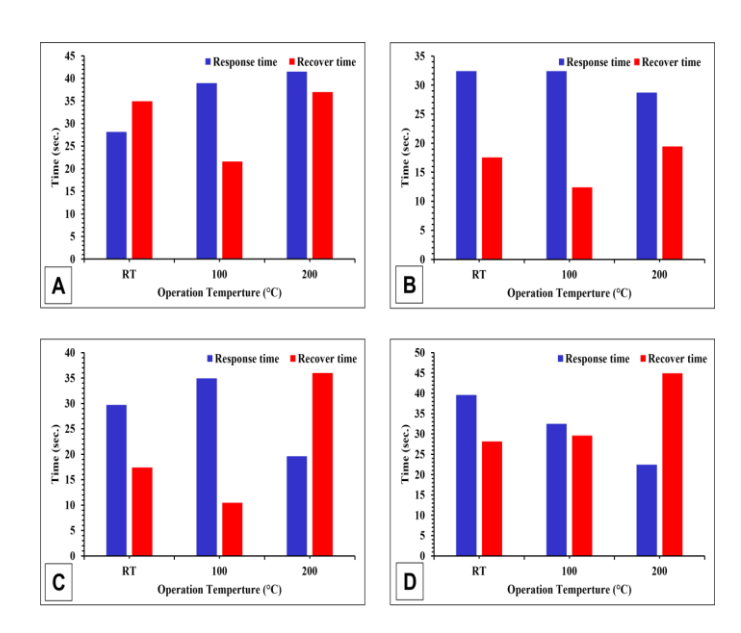


Figure 18. Response and recovery time plotted with operation temperature for CuO/ZnO nanofilms: A: pure, B: (0.08 wt.%), C: (0.14 wt.%), and D: (0.20 wt.%) at 500 ppm concentration for NH₃ Gas-detector for RT

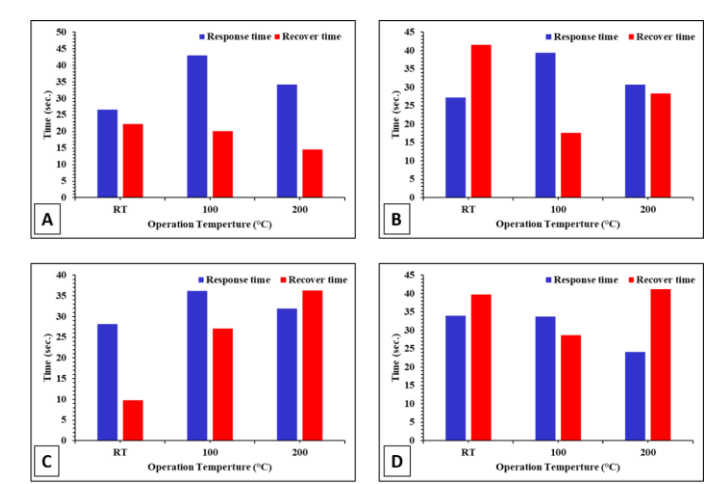


Figure 19. Response and recovery time plotted with operation temperature for CuO/ZnO nanofilms: A: pure, B: (0.08 wt.%), C: (0.14 wt.%), and D: (0.20 wt.%) at 500 ppm concentration for NH₃ Gas-detector for 573 K

desorption processes on the sensor's surface. As a result, the sensor exhibits improved sensitivity and operational reliability. Optimizing both response and recovery times significantly enhances the practicality and performance of gas sensing systems.

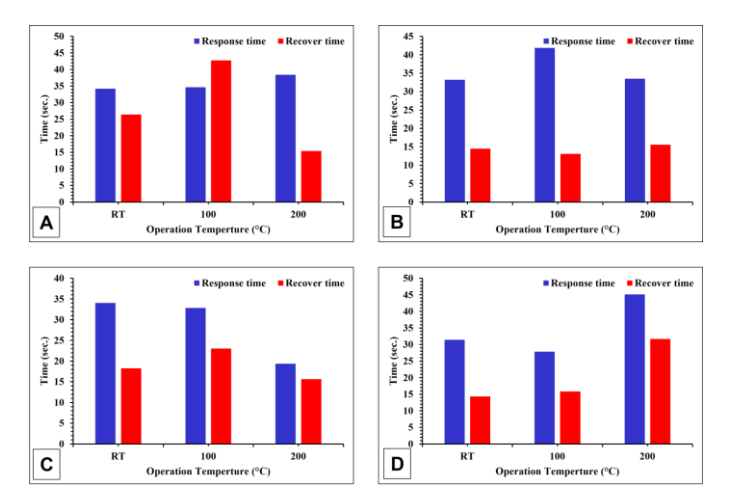


Figure 20. Response and recovery time plotted with operation temperature for CuO/ZnO nanofilms: A: pure, B: (0.08 wt.%), C: (0.14 wt.%), and D: (0.20 wt.%) at 500 ppm concentration for NH₃ Gas-detector for 673 K

The practical results of the proposed research were compared for the best sensitivity between before annealing at room temperature and after annealing at $573~\rm K$ and $673~\rm K$ as presented in Table 6 to show the most important results and improvements obtained during the research.

Table 3. The Gas-detector properties of CuO/ZnO nanofilms at RT indicate the presence of NH₃ gas

Conc. of ZnO doping	Operation	Sensitivity	Response time	Recover time
CuO (wt.%)	Temperature (°C)	(%)	(sec)	(sec)
	RT	02.23	28.17	34.92
(Pure-CuO RT)	100	16.60	38.97	21.60
	200	08.21	41.49	36.99
	RT	04.92	32.40	17.55
0.08 wt.%	100	28.17	32.40	12.42
	200	09.93	28.71	19.44
0.14 wt.%	RT	05.00	29.70	17.37
	100	37.61	34.92	10.44
	200	11.43	19.00	36.00
0.20 wt.%	RT	07.19	39.60	28.17
	100	47.29	32.49	29.61
	200	14.86	22.41	44.91

Table 4. The Gas-detector properties of CuO/ZnO nanofilms at 573 K indicate the presence of NH₃ gas

Conc. of ZnO doping CuO (wt.%)	Operation Temperature (°C)	Sensitivity (%)	Response time (sec)	Recover time (sec)
	RT	05.22	26.55	22.23
(Pure-CuO RT)	100	13.92	42.93	20.07
	200	10.67	34.20	14.58
	RT	02.85	27.27	41.58
0.08 wt.%	100	22.13	39.33	17.64
	200	08.09	30.78	28.35
0.14 wt.%	RT	05.12	28.17	09.81
	100	36.10	36.18	27.09
	200	09.69	31.95	36.27
0.20 wt.%	RT	06.57	34.02	39.78
	100	45.05	33.75	28.62
	200	19.87	24.12	41.22

Table 5. The Gas-detector properties of CuO/ZnO nanofilms at 673 K indicate the presence of NH₃ gas

Conc. of ZnO doping CuO (wt.%)	Operation Temperature (°C)	Sensitivity (%)	Response time (sec)	Recover time (sec)
	RT	13.72	34.20	26.37
(Pure-CuO RT)	100	19.37	34.65	42.75
	200	16.39	38.43	15.39
	RT	13.82	33.21	14.49
0.08 wt.%	100	34.43	41.85	13.05
	200	38.31	33.48	15.57
0.14 wt.%	RT	17.07	34.02	18.27
	100	48.21	32.85	23.04
	200	53.46	19.35	15.66
0.20 wt.%	RT	18.38	31.41	14.31
	100	68.81	27.81	15.84
	200	58.70	45.09	31.68

Table 6. The comparison of the proposed work between RT, 573 K, and 673 K for NH₃ Gas-detector

Conc. of ZnO doping CuO (wt.%)	Operation Temperature (°C)	Sensitivity (%)	Response time (sec)	Recover time (sec)
0.20wt.% at RT	100	47.29	32.49	29.61
0.20wt.% at 573K	100	45.05	33.75	28.62
0.20wt.% at 673K	100	68.81	27.81	15.84

4. CONCLUSION

This paper describes the preparation of nanofilms using pure CuO and ZnO-doped CuO with different contents (0. 0.8, 0.14, 0.20 wt.%) deposited on glass substrates. At room temperature (RT). The deposited nanofilms exhibit no discernible peaks in XRD examination. The widening of the peak indicates a lack of long-range symmetry, resulting in a disordered nanocrystal line structure. Thin film AFM pictures showed a constant granular surface shape. As ZnO doping increased, the roughness average and root mean square increased. The optical characteristics of CuO/ZnO show the absorbance and absorption coefficient augment with the rise in ZnO concentration. As the concentration of ZnO increased, the energy band gaps and transmittance decreased, which absorbed UV radiation. A direct energy gap (Eg) reduced from 3.610 to 3.487 eV when ZnO doping increased in the optical test of pure and Cu-doped ZnO nanofilms. The negative correlation between electrical resistance and time indicates p-type semiconducting nanofilm sensors. Gas detectors with a thin CuO/ZnO layer performed better at 100°C. In gas detection, the higher sensitivity was 47.29% at RT, the higher sensitivity was 45.05% at 573 K, and the higher sensitivity was 68.81% at 673 K in the study. NH₃ gas raised operating temperature. Followed by faster response and recovery.

ACKNOWLEDGMENTS

The authors would like to express appreciation and thanks to the anonymous editors and reviewers of the journal. In addition, the authors thanks Babylon University, Iraq, for their support.

REFERENCES

- [1] R. Chandra and S. Nimesh, *Theory, Techniques and Applications of Nanotechnology in Gene Silencing*, vol.
 2. New York: River Publishers, 2022. doi: 10.1201/9781003357193.
- [2] R. Tantra, *Nanomaterial characterization: An introduction*. John Wiley & Sons, 2016.
- [3] Y. Ju-Nam and J. R. Lead, "Manufactured nanoparticles: An overview of their chemistry, interactions and potential environmental implications," *Science of The Total Environment*, vol. 400, no. 1–3, pp. 396–414, 2008, doi: 10.1016/j.scitotenv.2008.06.042.
- [4] Y. Li and G. A. Somorjai, "Nanoscale Advances in Catalysis and Energy Applications," *Nano Letters*, vol. 10, no. 7, pp. 2289–2295, 2010, doi: 10.1021/nl101807g.
- [5] M. H. Meteab, A. Hashim, and B. H. Rabee, "Synthesis and Structural Properties of (PS-PC/Co₂O₃-SiC) Nanocomposites for Antibacterial Applications," *Nanosistemi, Nanomateriali, Nanotehnologii*, vol. 21, no. 2, pp. 451–460, 2023, doi: 10.15407/nnn.21.02. 451.
- [6] V. Khoramshahi, M. Azarang, M. Nouri, A. Shirmardi, and R. Yousefi, "Metal oxide/g-C₃N₄ nanocomposites chemiresistive gas sensors: A review on enhanced performance," *Talanta Open*, vol. 9, p. 100290, 2024, doi: 10.1016/j.talo.2024.100290.
- [7] F. Hussain and M. Meteab, "Nuclear reaction analyses for green chemistry: Evaluating environmental safety in charged particle interactions," *E3S Web of Conferences*, vol. 614, p. 04025, 2025, doi:

- 10.1051/e3sconf/202561404025.
- [8] N. A. Ibrahim, "Nanomaterials for Antibacterial Textiles," in *Nanotechnology in Diagnosis, Treatment and Prophylaxis of Infectious Diseases*, Elsevier, 2015, pp. 191–216. doi: 10.1016/B978-0-12-801317-5.00012-8.
- [9] Z. Yang, H. Peng, W. Wang, and T. Liu, "Crystallization behavior of poly(ε-caprolactone)/layered double hydroxide nanocomposites," *Journal of Applied Polymer Science*, vol. 116, no. 5, pp. 2658–2667, 2010, doi: 10.1002/app.31787.
- [10] S. Murthy, P. Effiong, and C. C. Fei, "Metal oxide nanoparticles in biomedical applications," in *Metal Oxide Powder Technologies*, Elsevier, 2020, pp. 233–251. doi: 10.1016/B978-0-12-817505-7.00011-7.
- [11] M. K. Mohammed, T. N. Khudhair, K. S. Sharba, A. Hashim, Q. M. Hadi, and M. H. Meteab, "Tuning the Morphological and Optical Characteristics of SnO₂/ZrO₂ Nanomaterials Doped PEO for Promising Optoelectronics Applications," *Revue des Composites et des Matériaux Avancés*, vol. 34, no. 4, pp. 495–503, 2024, doi: 10.18280/rcma.340411.
- [12] G. A. Kontos *et al.*, "Electrical relaxation dynamics in TiO₂–polymer matrix composites," *Express Polymer Letters*, vol. 1, no. 12, pp. 781–789, 2007, doi: 10.3144/expresspolymlett.2007.108.
- [13] J. Lillo-Ramiro *et al.*, "Optical and microstructural characteristics of CuO thin films by sol gel process and introducing in non-enzymatic glucose biosensor applications," *Optik*, vol. 229, p. 166238, 2021, doi: 10.1016/j.ijleo.2020.166238.
- [14] R. Nayak *et al.*, "Fabrication of CuO nanoparticle: An efficient catalyst utilized for sensing and degradation of phenol," *Journal of Materials Research and Technology*, vol. 9, no. 5, pp. 11045–11059, 2020, doi: 10.1016/j.jmrt.2020.07.100.
- [15] M. Grigore, E. Biscu, A. Holban, M. Gestal, and A. Grumezescu, "Methods of Synthesis, Properties and Biomedical Applications of CuO Nanoparticles," *Pharmaceuticals*, vol. 9, no. 4, p. 75, 2016, doi: 10.3390/ph9040075.
- [16] C. Wang, X. Q. Fu, X. Y. Xue, Y. G. Wang, and T. H. Wang, "Surface accumulation conduction controlled sensing characteristic of p-type CuO nanorods induced by oxygen adsorption," *Nanotechnology*, vol. 18, no. 14, p. 145506, 2007, doi: 10.1088/0957-4484/18/14/145506.
- [17] N. Mukherjee *et al.*, "CuO nano-whiskers: Electrodeposition, Raman analysis, photo-luminescence study and photocatalytic activity," *Materials Letters*, vol. 65, no. 21–22, pp. 3248–3250, 2011, doi: 10.1016/j.matlet.2011.07.016.
- [18] A. Moezzi, A. M. McDonagh, and M. B. Cortie, "Zinc oxide particles: Synthesis, properties and applications," *Chemical Engineering Journal*, vol. 185–186, pp. 1–22, Mar. 2012, doi: 10.1016/j.cej.2012.01. 076.
- [19] R. Chen, Z. Li, and W. Gao, "Effect of substrate on the morphology, crystal structure and property of ZnO thin films," *Asia-Pacific Journal of Chemical Engineering*, vol. 2, no. 5, pp. 388–393, 2007, doi:

- 10.1002/apj.70.
- [20] H. S. Suhail and A. R. Abdulridha, "Synthesis, optical and AC electrical characteristics of nanocomposites (Bi₂O₃/ZnO) films prepared by thermal evaporation technique," *Digest Journal of Nanomaterials and Biostructures*, vol. 18, no. 2, pp. 437–450, 2023, doi: 10.15251/DJNB.2023.182.437.
- [21] S. Liu, B. Yu, H. Zhang, T. Fei, and T. Zhang, "Enhancing NO₂ gas sensing performances at room temperature based on reduced graphene oxide-ZnO nanoparticles hybrids," *Sensors and Actuators B: Chemical*, vol. 202, no. 2, pp. 272–278, 2014, doi: 10.1016/j.snb.2014.05. 086.
- [22] J. Wang, P. C. Shih, and J. M. Carroll, "Revisiting Linus's law: Benefits and challenges of open source software peer review," *International Journal of Human-Computer Studies*, vol. 77, pp. 52–65, 2015, doi: 10.1016/j.ijhcs.2015.01.005.
- [23] S. M. Mali *et al.*, "Heterostructural CuO–ZnO Nanocomposites: A Highly Selective Chemical and Electrochemical NO₂ Sensor," *ACS Omega*, vol. 4, no. 23, pp. 20129–20141, 2019, doi: 10.1021/acsomega. 9b01382.
- [24] S. Jain, N. Karmakar, A. Shah, and N. G. Shimpi, "Development of Ni doped ZnO/polyaniline nanocomposites as high response room temperature NO2 sensor," *Materials Science and Engineering: B*, vol. 247, p. 114381, 2019, doi: 10.1016/j.mseb.2019. 114381.
- [25] R. Kumar, W. Zheng, X. Liu, J. Zhang, and M. Kumar, "MoS₂-Based Nanomaterials for Room-Temperature Gas Sensors," *Advanced Materials Technologies*, vol. 5, no. 5, pp. 1–28, 2020, doi: 10.1002/admt.201901062.
- [26] X. Liu, T. Ma, N. Pinna, and J. Zhang, "Two-Dimensional Nanostructured Materials for Gas Sensing," *Advanced Functional Materials*, vol. 27, no. 37, pp. 1–30, 2017, doi: 10.1002/adfm.201702168.
- [27] C. Dong, R. Zhao, L. Yao, Y. Ran, X. Zhang, and Y. Wang, "A review on WO₃ based gas sensors: Morphology control and enhanced sensing properties," *Journal of Alloys and Compounds*, vol. 820, p. 153194, 2020, doi: 10.1016/j.jallcom.2019.153194.
- [28] A. Dey, "Semiconductor metal oxide gas sensors: A review," *Materials Science and Engineering: B*, vol. 229, 2017, pp. 206–217, 2018, doi: 10.1016/j.mseb. 2017.12.036.
- [29] N. Yamazoe, G. Sakai, and K. Shimanoe, "Oxide semiconductor gas sensors," *Catalysis Surveys from Asia*, vol. 7, no. 1, pp. 63–75, 2003, doi: 10.1023/A:1023436725457.
- [30] S. Poongodi *et al.*, "Electrodeposition of WO₃ nanostructured thin films for electrochromic and H_2S gas sensor applications," *Journal of Alloys and Compounds*, vol. 719, pp. 71–81, 2017, doi: 10.1016/j.jallcom.2017.05.122.
- [31] H. J. Nam, T. Sasaki, and N. Koshizaki, "Optical CO gas sensor using a cobalt oxide thin film prepared by pulsed laser deposition under various argon pressures," *The Journal of Physical Chemistry B*, vol. 110, no. 46, pp. 23081–23084, 2006, doi: 10.1021/jp063484f.

- [32] T. Anukunprasert, C. Saiwan, and E. Traversa, "The development of gas sensor for carbon monoxide monitoring using nanostructure of Nb-TiO₂," *Science and Technology of Advanced Materials*, vol. 6, no. 3–4, pp. 359–363, 2005, doi: 10.1016/j.stam.2005.02.020.
- [33] N. A. Hassan and I. H. Khudayer, "Study of the structural and optical properties of CuAl_xIn_{1-x}Te₂ thin film," *AIP Conference Proceedings*, vol. 2190, no. 1, 2019, p. 020050, doi: 10.1063/1.5138536.
- [34] D. J. Klotzkin, *Introduction to Semiconductor Lasers for Optical Communications*. Cham: Springer International Publishing, 2020. doi: 10.1007/978-3-030-24501-6.
- [35] A. Razzaq Abdul Ridha and N. A. Al-Isawi, "Studying the effect of annealing temperatures on the optical properties of CdS:1% Cu nanoparticles thin films prepared by thermal evaporation technique," *Journal of Physics: Conference Series*, vol. 1234, no. 1, p. 012029, 2019, doi: 10.1088/1742-6596/1234/1/012029.
- [36] S. Syed Zahirullah, J. Joseph Prince, and P. Fermi Hilbert Inbaraj, "Structural and optical properties of Cu-doped ZnO nanorods by silar method," *Materials Technology*, vol. 32, no. 12, pp. 755–763, 2017, doi: 10.1080/10667857.2017.1351656.
- [37] H. S. Suhail and B. H. Rabee, "New nanocomposites (PMMA-SPO-SiC) fabrication and of their structural and electrical properties for pressure sensors," in *AIP Conference Proceedings*, AIP Publishing, 2020, p. 020136. doi: 10.1063/5.0000093.
- [38] S. B. Jagadale *et al.*, "Nanorods to nanosheets structural evolution of $Ni_xZn_{1-x}O$ for NO_2 gas sensing application," *Journal of Alloys and Compounds*, vol. 766, pp. 941–951, 2018, doi: 10.1016/j.jallcom.2018. 07.040.
- [39] S. S. Al-Abbas *et al.*, "Influence of the polymer molecular weights on the electrical properties of Poly(vinyl alcohol) Poly(ethylene glycols)/ Graphene oxide nanocomposites," *Materials Today: Proceedings*, vol. 42, pp. 2469–2474, 2021, doi: 10.1016/j.matpr.2020.12.565.
- [40] W. K. Mahmood *et al.*, "Empowering NO₂ Detection: Synthesis of Highly Responsive Au/Cu-Doped Iron Oxide Nanoparticles as Gas Sensors Through Laser Ablation," *Plasmonics*, vol. 19, no. 6, pp. 3167–3176, 2024, doi: 10.1007/s11468-024-02235-2.
- [41] M. H. Sarfi, M. Ghadimi, and A. Babaee, "H₂S Gas Sensor Based on SnO₂ and CuO Nanoparticles," *STEM Fellowship Journal*, vol. 1, no. 2, pp. 21–26, 2015, doi: 10.17975/sfj-2015-012.
- [42] N. H. Harb and F. A. H. Mutlak, "Gas sensing characteristics of WO₃NPs sensors fabricated by pulsed laser deposition on PS n-type," *Journal of Optics*, vol. 52, no. 1, pp. 323–331, 2023, doi: 10.1007/S12596-022-00877-1.
- [43] S. N. Tarrad, S. A. Hussain, and F. H. Al-Asady, "Study of structural, optical and sensitivity properties of NiPc thin film prepared by thermal evaporation," *AIP Conference Proceedings*, vol. 2235, no. 1, p. 020036, 2020, doi: 10.1063/5.0008854.
- [44] S. Bates, G. Zografi, D. Engers, K. Morris, K. Crowley,

- and A. Newman, "Analysis of Amorphous and Nanocrystalline Solids from Their X-Ray Diffraction Patterns," *Pharmaceutical Research*, vol. 23, no. 10, pp. 2333–2349, Oct. 2006, doi: 10.1007/s11095-006-9086-2.
- [45] A. A. Attia, F. Sh. Hashim, and K. H. Abass, "Solar cell of Sb₂O₃:CuO/Si prepared via thermal evaporation technique: structural, morphological properties and efficiency," *Canadian Journal of Chemistry*, vol. 101, no. 10, pp. 813–820, 2023, doi: 10.1139/cjc-2023-0001.
- [46] L. Leontie, M. Caraman, M. Delibaş, and G. I. Rusu, "Optical properties of bismuth trioxide thin films," *Materials Research Bulletin*, vol. 36, no. 9, pp. 1629–1637, 2001, doi: 10.1016/S0025-5408(01)00641-9.
- [47] H. K. Obayes, M. H. Meteab, and B. A. Al-Kareem, "Modified Dosimetric Features of New Type of Lithium Borate Glass System: Role of Magnesium and Gold Co-doping," *Transactions on Electrical and Electronic Materials*, vol. 25, no. 6, pp. 708–721, 2024, doi: 10.1007/s42341-024-00551-2.
- [48] M. Yasin *et al.*, "Development of Bi₂O₃-ZnO heterostructure for enhanced photodegradation of rhodamine B and reactive yellow dyes," *Surfaces and Interfaces*, vol. 30, p. 101846, 2022, doi: 10.1016/j.surfin.2022.101846.
- [49] M. H. Naeem, S. H. H. Al-Nesrawy, and M. H. Al-Maamori, "Influence of Lead Nanoparticles on Structural, Morphological, and Mechanical Characteristics of (SiR-PU/Micro-Pb) Composites and Radiation Shielding Applications," East European Journal of Physics, no. 3, pp. 539–545, 2023, doi: 10.26565/2312-4334-2023-3-63.
- [50] R. Grazziotin-Soares *et al.*, "Effect of bismuth oxide on white mineral trioxide aggregate: chemical characterization and physical properties," *International Endodontic Journal*, vol. 47, no. 6, pp. 520–533, 2014, doi: 10.1111/IEJ.12181.
- [51] M. H. Meteab, A. Hashim, and B. H. Rabee, "Synthesis and tailoring the morphological, optical, electronic and photodegradation characteristics of PS-PC/MnO₂-SiC quaternary nanostructures," *Optical and Quantum Electronics*, vol. 55, no. 2, p. 187, 2023, doi: 10.1007/s11082-022-04447-4.
- [52] W. Gao and Z. Li, "ZnO thin films produced by magnetron sputtering," *Ceramics International*, vol. 30, no. 7, pp. 1155–1159, 2004, doi: 10.1016/ j.ceramint.2003.12.197.
- [53] L. Cong, X. Zheng, P. Hu, and S. Dan-feng, "Bi₂O₃ Vaporization in Microwave-Sintered ZnO Varistors," *Journal of the American Ceramic Society*, vol. 90, no. 9, pp. 2791–2794, 2007, doi: 10.1111/j.1551-2916. 2007.01848.x.
- [54] Ü. Özgür *et al.*, "A comprehensive review of ZnO materials and devices," *Journal of Applied Physics*, vol. 98, no. 4, p. 041301, 2005, doi: 10.1063/1.1992666.
- [55] A. Ghosh, N. Kumari, and A. Bhattacharjee, "Investigation on structural and optical properties of Cu doped ZnO," *Journal of Nanoscience and Nanotechnology*, vol. 2, no. 4, pp. 485–489, 2014, doi: 10.13140/2.1.2262.5929.

- [56] G. S. Ahmed, T. H. Mahmoud, H. I. Mohammed, and A. A. Hussein, "Fabrication and study of ZnO thin films using thermal evaporation technique," *Egyptian Journal of Chemistry*, vol. 64, no. 9, pp. 5189–5197, 2021, doi: 10.21608/ejchem.2021.71184.3563.
- [57] G. A. Somorjai and Y. Li, *Introduction to surface chemistry and catalysis*. John Wiley & Sons, 2010.
- [58] H. S. Suhail and A. R. Abdulridha, "Investigation of the Morphological, Optical, and D.C Electrical Characteristics of Synthesized (Bi₂O₃/ZnO) Nanocomposites, as Well as Their Potential Use in Hydrogen Sulfide Gas Sensor," *Transactions on Electrical and Electronic Materials*, vol. 24, no. 3, pp. 205–216, 2023, doi: 10.1007/s42341-023-00436-w.
- [59] S. Indris, P. Heitjans, M. Ulrich, and A. Bunde, "AC and DC Conductivity in Nano- and Microcrystalline Li₂O: B₂O₃ Composites: Experimental Results and Theoretical Models," *Zeitschrift für Physikalische Chemie*, vol. 219, no. 38353, pp. 89–103, 2005, doi:

- 10.1524/zpch.219.1.89.55015.
- [60] A. Hashim and Q. Hadi, "Structural, electrical and optical properties of (biopolymer blend/titanium carbide) nanocomposites for low cost humidity sensors," *Journal of Materials Science: Materials in Electronics*, vol. 29, no. 13, pp. 11598–11604, 2018, doi: 10.1007/s10854-018-9257-z.
- [61] A. Sawalha, M. Abu-Abdeen, and A. Sedky, "Electrical conductivity study in pure and doped ZnO ceramic system," *Physica B: Condensed Matter*, vol. 404, no. 8–11, pp. 1316–1320, 2009, doi: 10.1016/j.physb.2008. 12.017.
- [62] R. A. Abdul-Nabi and E. Al-Bermany, "Performers of Si₃N₄ Concentrations on Morphology and Electrical Behavior for New Quinary Fabrication PEO-CMC-PANI/GO@Si₃N₄ Nanocomposites for Electronic Devise and Gas Sensor Application," *Silicon*, vol. 16, no. 15, pp. 5583–5601, 2024, doi: 10.1007/s12633-024-03092-8.